Three-dimensional seismic structure of the Dragon Flag oceanic core complex at the ultraslow spreading Southwest Indian Ridge (49°39'E).

Minghui Zhao, Xuelin Qiu, Jiabiao Li, Daniel Sauter, Aiguo Ruan, John Chen, Mathilde Cannat, Satish Singh, Jiazheng Zhang, Zhenli Wu, et al.
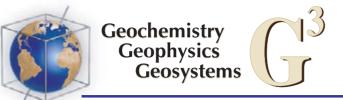
HAL Id: hal-00914264

https://hal.science/hal-00914264

Submitted on 9 Jun 2017

Three-dimensional seismic structure of the Dragon Flag oceanic core complex at the ultraslow spreading Southwest Indian Ridge (49°39′E)

Minghui Zhao and Xuelin Qiu
Key Laboratory of Marginal Sea Geology, South China Sea Institute of Oceanology, Chinese Academy of Sciences, Guangzhou, 510301, China (mhzhao@scsio.ac.cn)

Jiabiao Li
Second Institute of Oceanography, State Oceanic Administration , Hangzhou 310012 China (jbli@sio.org.cn)

Daniel Sauter
Institut de Physique du Globe de Strasbourg, CNRS-UMR 7516, Strasbourg, France

Aiguo Ruan
Second Institute of Oceanography, State Oceanic Administration, Hangzhou, China

John Chen
School of Earth and Space Sciences, Peking University, Beijing, China

Mathilde Cannat and Satish Singh
Laboratoire de Geoscience Marine, Institut de Physique du Globe de Paris, Paris, France

Jiazheng Zhang
Key Laboratory of Marginal Sea Geology, South China Sea Institute of Oceanology, Chinese Academy of Sciences, Guangzhou, 510301, China

University of Chinese Academy of Sciences, Beijing, China

Zhenli Wu and Xiongwei Niu
Second Institute of Oceanography, State Oceanic Administration, Hangzhou, China

[1] The Southwest Indian Ridge (SWIR) is an ultraslow spreading end-member of mid-ocean ridge system. We use air gun shooting data recorded by ocean bottom seismometers (OBS) and multibeam bathymetry to obtain a detailed three-dimensional (3-D) P wave tomographic model centered at 49°39′E near the active hydrothermal "Dragon Flag" vent. Results are presented in the form of a 3-D seismic traveltime inversion over the center and both ends of a ridge segment. We show that the crustal thickness, defined as the depth to the 7 km/s isovelocity contour, decreases systematically from the center (∼7.0–8.0 km) toward the segment ends (∼3.0–4.0 km). This variation is dominantly controlled by thickness changes in the lower crustal layer. We interpret this variation as due to focusing of the magmatic activity at the segment center. The across-axis velocity model documents a strong asymmetrical structure involving oceanic detachment faulting. A locally corrugated oceanic core complex (Dragon Flag OCC) on the southern ridge flank is characterized by high shallow crustal velocities and a strong vertical velocity gradient. We infer that this OCC may be predominantly made of gabbros. We suggest that detachment faulting is a prominent process of slow spreading oceanic crust accretion even in magmatically robust ridge sections. Hydrothermal activity at the Dragon Flag vents is located next to the

detachment fault termination. We infer that the detachment fault system provides a pathway for hydrothermal convection.

1. Introduction

[2] The discovery of widespread detachment faulting on the Mid Atlantic Ridge (MAR) revealed that not only volcanic but also tectonic processes play a central role in the accretion of slow spreading oceanic lithosphere [*Cannat*, 1993; *Tucholke and Lin*, 1994; *Tucholke et al.*, 1998; *Escartín et al.*, 2008]. The footwalls of long-lived, extensional faults, called oceanic core complexes (OCCs), can accommodate more than 50% of total plate separation [*Tucholke et al.*, 2008; *Olive et al.*, 2010], expose mantle peridotites, and large volumes of gabbroic rocks and produce gentle domal structures [*Smith et al.*, 2006]. Hydrothermal activity identified so far along the northern MAR is also closely associated with detachment faults [*Escartín et al.*, 2008]. Recent modeling of OCCs suggested that tectonic and magmatic processes are not decoupled and that oceanic detachments require small but significant magma supply to form [*Tucholke et al.*, 2008]. However, the real extent of tectonic-dominated spreading, the geometry of faults at depth, and the link between deformation, magmatic emplacement, and hydrothermal circulation are still poorly known, especially at ultraslow spreading ridges.

[3] The first high-temperature hydrothermal field discovered on an ultraslow spreading ridge was found at the Southwest Indian Ridge (SWIR) during Chinese cruise DY115-19 in 2007 [*Tao et al.*, 2012]. Magnetic data reveal a well-defined low crustal magnetization zone near the Dragon Flag hydrothermal vent [*Zhu et al.*, 2010], which is larger in size than the Trans-Atlantic Geotraverse

(TAG) hydrothermal mound on the MAR [*Rona et al.*, 1986; *Humphris and Kleinrock*, 1996]. This newly discovered field together with other previous observations at ultraslow spreading Arctic ridges shows that the SWIR and the Arctic ridges exhibit unique hydrothermal systems, and that the distribution of vents along mid-oceanic ridges is not a simple function of spreading rate [*German et al.*, 1998; *Baker and German*, 2004]. The SWIR exhibits large along-axis variations of magma supply [*Cannat et al.*, 2008] with an ultraslow spreading rate varying only slightly along the 7700 km ridge axis (12–16 mm/yr) [*Chu and Gordon*, 1999]. It is therefore an ideal place to study the role of the magma budget versus the tectonic processes on the hydrothermal circulation.

[4] Large "low-angle" normal faults [*Karson et al.*, 1987] or detachment faults passing through the axial lithosphere [*Cannat*, 1993] were postulated to explain exposure of gabbros and peridotites at slow spreading ridges. *Tucholke and Lin* [1994] proposed a geologic model in which detachment faults could be very long-lived at the inside corners of ridge-transform intersections based on analysis of gravity and seafloor samples of the MAR. Footwalls of these long-lived faults form OCCs [*Karson and Lawrence*, 1997] and corrugated dome-shaped surfaces were recognized in the form of megamullions [*Cann et al.*, 1997; *Tucholke et al.*, 1998]. It has been recently recognized that detachment faulting is a fundamental mode of accretion for the oceanic lithosphere [*Escartín and Canales*, 2011; *Escartín et al.*, 2008; *Smith et al.*, 2006]. Corrugated OCCs have been identified and analyzed in the easternmost SWIR (64°E) using topography and gravity

signature [*Cannat et al.*, 2009]. However, no observations of OCCs and detachment faults have yet been presented in the more-magmatic part of SWIR.

[5] Data were sparse up to the 1980s for the Arctic Ridge and the SWIR largely because of logistical issues, both ridges being located in regions that experience some of the most extreme weather in the world. During the last two decades, along-axis surveys revealed striking contrasts between the ultraslow spreading SWIR and faster spreading ridges, the most notable difference being the apparent absence of volcanic activity on long stretches of ridge where large expanses of mantle-derived peridotites are exposed at the seafloor [*Dick et al.*, 2003; *Sauter et al.*, 2004; *Seyler et al.*, 2003]. The easternmost part of the SWIR was shown to be among the deepest parts of the oceanic ridge system, and it was thus inferred to represent a melt poor end-member [*Cannat et al.*, 1999]. This region displays the widest expanses known to date of seafloor with no evidence for a volcanic upper crustal layer [*Cannat et al.*, 2006]. However, much less attention was paid to the central, shallower and more-magmatic part of the SWIR [*Georgen et al.*, 2001; *Sauter et al.*, 2001]. Their thicker crust is thought to be produced by a melting anomaly possibly related to the Crozet hotspot [*Sauter et al.*, 2009]. Only two cruises have been devoted to the seismic structure of the SWIR, one is the cruise RRS DISCOVERY 208 in 1994 including two survey areas at 66°E and at 57°E close to the Atlantis II Transform Fault (TF) [*Muller et al.*, 1997, 1999, 2000; *Minshull and White*, 1996; *Minshull et al.*, 2006], the other one is the 2008 Hakuho-maru KH-07-4 seismic cruise at 37°E close to the Marion Island (http://www.inter ridge.org/de/node/5452). Seismic data were thus needed to better constrain the variations and changes in the crustal velocity structure in this central magmatic part of the ultraslow spreading SWIR.

[6] In this paper, we report an extensive ocean bottom seismometers (OBS) experiment that was carried out in 2010 at the SWIR segment that hosts the active Dragon Flag hydrothermal vent (37°47′S, 49°39′E). We present a detailed study of the 3-D velocity structure of the oceanic crust formed in this region of the SWIR, document geologic structure of an OCC in the area, infer crustal composition from the results, and note a possible association between crustal structure and the active hydrothermal system.

2. Geological Setting of the Study Area

[7] The SWIR forms the boundary between the Antarctic plate to the south and the African plate to the north (Figure 1a), and extends from the Bouvet triple junction (BTJ) in the west to the Rodrigues triple junction (RTJ) in the east [*Patriat et al.*, 1997; *Muller et al.*, 2000; *Georgen et al.*, 2001]. Regional shallow axial depths, negative Mantle Bouguer Anomalies (MBA), low basalt Na8.0 content (a geochemical proxy for the extent of partial melting) [*Cannat et al.*, 2008, Figure 1], and a negative anomaly of S wave velocities in the surface wave tomography of *Debayle et al.* [2005], all indicate the presence of thicker crust and/or hotter mantle between the Indomed TF and Gallieni TF (46°00′E and 52°20′E) relative to the deeper eastern and western ridge sections [*Cannat et al.*, 2008]. Seafloor accreted between these transform faults over the past ~10 Myr is also locally much shallower (>1000 m) than previously accreted seafloor along the same ridge region. Gravity data suggest that this anomalously shallow area corresponds to >1.7 km thicker crust [*Sauter et al.*, 2009]. This area has been interpreted as a volcanic plateau due to a sudden increase of the magma supply that may be ascribed to a regionally higher mantle temperature provided by mantle migration from the Crozet hotspot toward the SWIR [*Sauter et al.*, 2009].

[8] The ridge segment between the Indomed TF and the Gallieni TF is oblique with respect to the direction of plate motion (overall 15° obliquity) (Figure 1b). Indomed TF (~20 Myr) and Gallieni TF (~16 Myr) offset the ridge by about 145 and 115 km, respectively. No other transform fault is observed and the obliquity of the ridge segment results from several nontransform discontinuities (NTDs) [*Rommevaux-Jestin et al.*, 1997]. Our survey area (Figure 1b) includes segment 27 and 28 (following the nomenclature of *Cannat et al.* [1999]) limited by three NTDs. Segment 27 has been interpreted as a magmatically robust segment: it is 90 km long and is associated with a high along-axis relief and a large MBA low. Segment 27 culminates at <1500 m in part of the ridge characterized by numerous flat topped seamounts [*Sauter et al.*, 2001]. Between segment 27 and 28, a deep NTD which offsets the axis by 10 km is observed with a single small basin. There, gravity data suggest that the crust at segment centers is on average 2–3 km thicker crust than the crust at NTDs [*Mendel et al.*, 2003]. With a much smaller along-axis relief and MBA low, segment

28 is thought to be magmatically weaker than segment 27. There are no clear off-axis traces of the ends of segment 28 in the bathymetric data nor in the gravity data, suggesting that this segmentation has not been stable in time. It has been suggested that the magma supply to this low-relief segment 28 is controlled by the melt migration and/or crustal plumbing from the adjacent high-relief
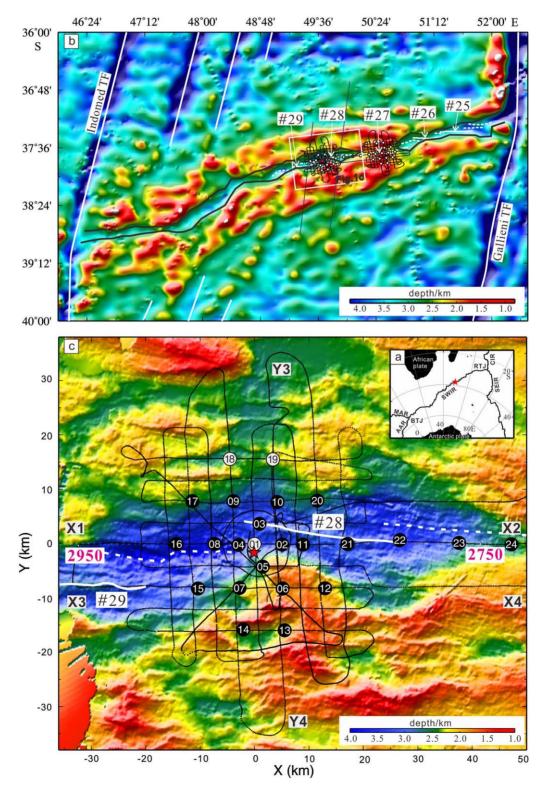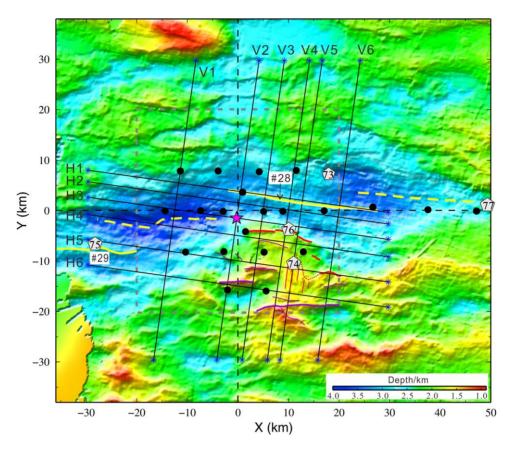

Figure 1.

Figure 2. Shaded-relief image centered on segment 28. Black solid circles are shown the positions of OBSs. The solid yellow line represents NVR for the spreading segments 28 and dash yellow lines along the deepest points of the NTDs as defined by *Sauter et al.* [2001, 2004]. The pink star indicates the Dragon Flag hydrothermal vent. The 73–77 pentangles are the locations of dredge hauls. The black lines locate the H1–H6 and V1–V6 sections in Figures 5 and 6 and supporting information Figures S2 and S3, which are parallel and perpendicular to the spreading axis of Segment 28, respectively. Note the prominent approximately north fault slips composing the corrugated structure. The breakaway of the detachment faults are marked in bold purple lines, the termination in thick red lines, and the corrugated region in thinner red lines. Same meanings are for Figures 5–7 and Figure 10. The dash gray square indicates the domain of slices in Figure 7.

segment 27 [*Sauter et al.*, 2001]. This paper focuses on the tomography results obtained at segment 28 (Figure 1c).

[9] Segment 28 presents a highly asymmetric topography: the southern ridge flank is relatively shallow (<2000 m deep) and locally bears corrugations typical of OCCs (Figure 2). The northern ridge flank has a deeper topography (>2000 m). The southern domain extends about 5 km along-axis. It faces a robust neo-volcanic ridge (NVR) that extends along-axis from the bottom of the eastern NTD basin to the northern rift valley wall of the western NTD (Figure 2). Figure 2 shows a

Figure 1. (a) Map of the study area along the SWIR. (b) Bathymetric and structural map of the SWIR between 46°E and 52°E. The fracture zones (white lines) and axial valley (bold black lines) are from *Sauter et al.* [2001]; tracks of 3-D seismic OBS survey are shown in thin black lines; the white square is the domain of Figure 1c; (c) Bathymetry map of segment 28 in Cartesian Coordinates (origin of the local coordinate system corresponds to 49.65157°E, 37.76852°S. The positions of OBSs (closed black circles) and air gun shooting tracks (black points) are shown, white circles indicate lost and no-data OBSs. White lines represent the axis: solid along the neo-volcanic ridge (NVR) in the spreading segments of 28 and 29, and dash white lines along the deepest points of the NTDs as defined by *Sauter et al.* [2001, 2004]. The red star indicates the location of active Dragon Flag hydrothermal vent. The shooting line X1X2 defines the horizontal axis orientation (8° clockwise from North). The red shot numbers are corresponding to the seismic sections in Figure 3. Line Y3Y4 corresponds to the model of Figure 8.

structural sketch of the inferred OCC structure in the southern ridge flank, based on multibeam bathymetry [*Patriat et al.*, 1996]. We named it the Dragon Flag OCC because it is close to the hydrothermal field of the same name. The corrugated area extends some 5 km along-axis and 6 km in the spreading direction. It is part of a longer and wider domal structure that ends to the south in a series of steep scarps that have morphology typical of detachment fault breakaways [e.g., *Smith et al.*, 2006, 2008]. To the north, the domal and locally corrugated structure ends at or next to the axial valley wall that presents significantly steeper slopes and is therefore interpreted as a termination fault, i.e., the high-angle fault achieved by a uplift at the termination stage, when the corrugated surface exposed at the seafloor has been flexurally tilted away from the axis.

3. Seismic Experiment and Data Processing

[10] A three-dimensional (3-D) seismic survey was carried out on the SWIR from January to March 2010 during the DY115-21 global cruise of *R/V* Dayang Yihao. The seismic source was a four-air gun array, which was towed at a depth of ~10 m with a total volume of 6000 cubic inches (or 98.32 L) and a firing air pressure of 120–130 kg/cm^2. It was fired at a shooting interval of 100–130 s providing a seismic trace spacing of ~250 m at a nominal speed of 5 knots (9.25 km/h). A total of 10,832 shots were fired and 52 survey lines (about 2650 km in length) were completed. Shooting track lines form two boxes which are connected by main lines X1X2 and X3X4 covering the entire length of ridge segments 27 and 28 (Figure 1). Shot positions were Global Positioning System (GPS) navigated, and corrected for the distance between the GPS antenna on the ship and the center of the air gun array in the water [*Ao et al.*, 2010]. Due to three suites of advanced timing clock equipped onboard, the error of the shooting time is less than 1 ms [*Ao et al.*, 2010].

[11] Forty OBSs (with three-component geophones and hydrophone) were deployed for recording air gun signals (Figure 1c). Two OBSs (OBS19, OBS28) were lost, while another two OBSs (OBS01, OBS18) returned no useful data (Figure 1c). The seismic data were recorded by three types of OBSs (Chinese, German, and French) at sample intervals of 125, 250, and 125 Hz, respectively [*Zhang et al.*, 2012]. We focus here on the OBS data in the western box and will present tomographic imaging centered on the active Dragon Flag hydrothermal vent (Figure 1c). This box is approximately 80 × 60 km^2 in area, and seismic ray coverage extends to 7–8 km depth beneath the seafloor. The locations of the OBS instruments on the seafloor were determined by inverting the direct water-wave travel times using the Monte Carlo method and least square method, which yielded error estimates within 10–20 m [*Ao et al.*, 2010]. The water depths at the relocated positions were obtained from multibeam bathymetry measurement simultaneously during the shooting operation.
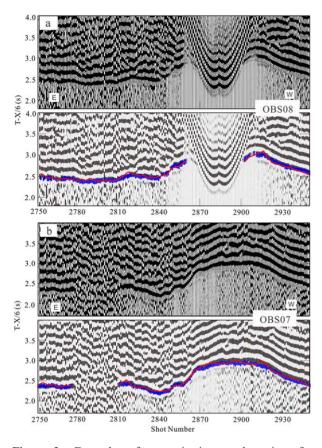
[12] The seismic data were reduced to the standard format of the Society of Exploration Geophysicist (SEGY). We concentrate exclusively on *P* wave first arrivals for each OBS in this study. We pick first-arrival travel times manually in band-pass filtered (5–20 Hz) record sections for the hydrophone component (sometimes vertical component) without differencing between crustal and mantle refracted phases (*Pg* and *Pn*), and excluding direct water-wave phases (Figure 3). Observed travel time uncertainties were calculated based on the signal-to-noise ratio (SNR) [e.g., *Zelt and Forsyth*, 1994]. In addition, travel time uncertainties included a constant value of 30 ms to account for uncertainty in seafloor ray entry point in areas with large topographic changes. In total we picked 65,634 first-arrival travel times from 20 OBSs' record sections.

4. Modeling Method and Results

4.1. Tomography Method

[13] We used the iterative first-arrival seismic tomography approach (FAST) of *Zelt and Barton* [1998] to construct a smooth, isotropic 3-D *P* wave velocity model of the 28 ridge segment. The choice of the starting model is an important step in tomography. We build the one-dimensional (1-D) velocity model which is draped from the seafloor in order to construct the starting 3-D volume. The seafloor interface was constructed from multibeam bathymetry data acquired during the experiment. Velocity in the water layer was kept to 1.5 km/s. We tried to get a solution with the least amount of required structure that fits the observed travel times adequately (low root-mean-square (RMS) and χ^2 close to 1 ideally) in the least number of iterations. This is accomplished by normalizing all regularized operators by the slowness of the

Figure 3. Examples of two seismic record sections for instruments (a) OBS08 and (b) OBS07 showing X1X2 shooting recordings (shots 2750–2950 in Figure 1). The section of OBS07 is off-line shooting showing no direct water wave. Data have been band-pass filtered between 5 and 20 Hz, and amplitudes have been scaled according to range for display purposes. (bottom) Observed travel times (blue vertical bars with length equal to the assigned travel time uncertainty) and calculated travel times (the red line) predicted by the final model.

starting model, linearizing by damped least squares solution (LSQR) [*Zelt and Barton*, 1998]. Lambda (λ) is a trade-off parameter that controls the relative weighting of fitting the travel time data versus solution constraints, and the parameter alpha (α) controls the relative importance of smoothness/flatness versus smallest perturbation within the regularization part. We run a number of inversions to find the appropriate λ value as well as the appropriate value of the horizontal grid node spacing for the inverse problem (D_{xy}).

[14] The forward problem (ray path and travel time calculations) is solved on this 3-D volume parameterized with a uniform square node spacing of 250 m in X, Y, and Z directions. A relatively dense parameterization of 305×313 horizontal nodes in an area of 76 km $\times$ 78 km and 53 vertical

nodes from 0 to 13 km below the seafloor is used (5,059,645 spacing nodes in total arranged in a regular grid). The inverse problem uses a volume with 500 m cell spacing in the two horizontal directions (152×156 cells) and in the vertical direction (26) (616,512 cells in total).

[15] Travel times calculated by this 3-D structure fit the data poorly ($\chi^2 > 25$; Figure 4a) with residuals ranging between -500 and 500 ms, and larger positive (blue) and negative (red) residuals in the first inversion (Figure 4c). After four iterations, results show that the combination of $\lambda = 1$, $D_{xy} = 250$ m, and $\alpha = 0.95$ provides the best fit to the data with a RMS misfit of 52 ms and a corresponding normalized misfit $\chi^2 = 1.36$ (Figure 4b). All instruments and shots are equally well fit (i.e., travel time residuals do not show dependence on shot number or OBS number, Figure 4d). The travel time residuals are independent to source-receiver offsets, indicating that observed data equally fit well at all offsets (Figure 4e).

4.2. Preferred P Wave Velocity Model

[16] Any solution to the inverse problem depends on the starting model chosen to a certain degree, and a complete solution must include a measurement of uncertainty. We followed a Monte Carlo approach similar to that of *Zhang et al.* [1998] and *Korenaga et al.* [2000] in order to account for the influence of the starting model on the solution and to obtain an estimate of the uncertainty. One hundred random 1-D starting models were constructed (see [1]supporting information) and 100 different inversions were performed. Assuming that the random initial models are independent of each other and that all solutions are equally valid, the average ensemble and the standard deviation of the 100 solutions are valid statistical estimates of the final model and its uncertainty [e.g., *Korenaga et al.*, 2000].

[17] The 100 inversions were performed using the same parameters, as described in the previous section. The average model of the final ensemble (preferred solution) is our preferred velocity model. The 3-D image of compressional wave (*P* wave) velocity in a 76 km $\times$ 78 km $\times$ 13 km volume shows the seismic structure centered on the Dagon Flag vent field in the segment 28 of SWIR. The resolution of the models is discussed in supporting information.
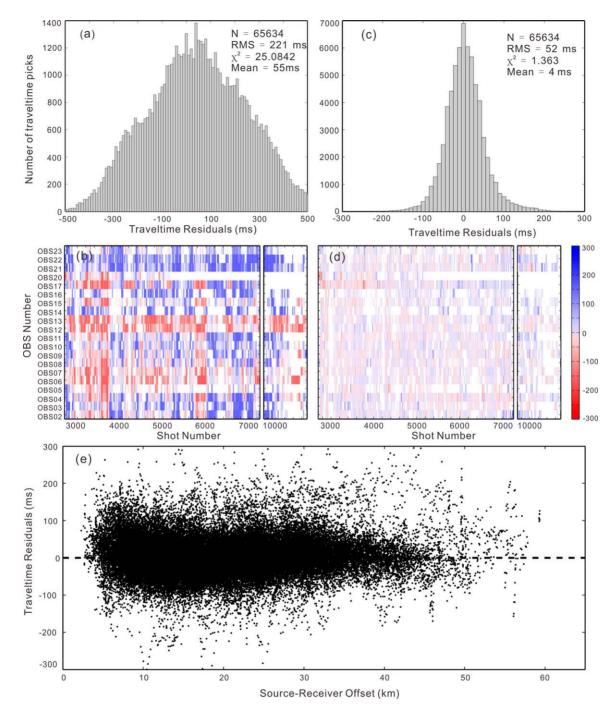
Figure 4. Histograms of travel time residuals calculated by (a) the initial 1-D model and (c) the final model. (b) and (d) Display color pictures of travel time residuals as a function of shot number and source, predicted by the initial 1-D model before inversion and by the final model, respectively. The vertical coordinate shows the OBS number, color scale illustrates the travel time residuals for each shot. (e) Travel time residuals of the final model as a function of source-receiver offset.

[18] Vertical slices in this 3-D model (Figures 5 and 6) are shown along selected spreading parallel (flow lines) and spreading perpendicular (along-axis lines) lines located in Figure 2. The plan view slices are focused on the central part of ridge segment 28 at 0.5–5 km depth below the seafloor (bsf; Figure 7). The velocity model from tomographic inversion is our primary result, from which the velocity gradient, velocity anomaly and velocity uncertainty models were derived and used to describe the variations of the velocity structure (Figures 5–7). Velocity gradients are useful to
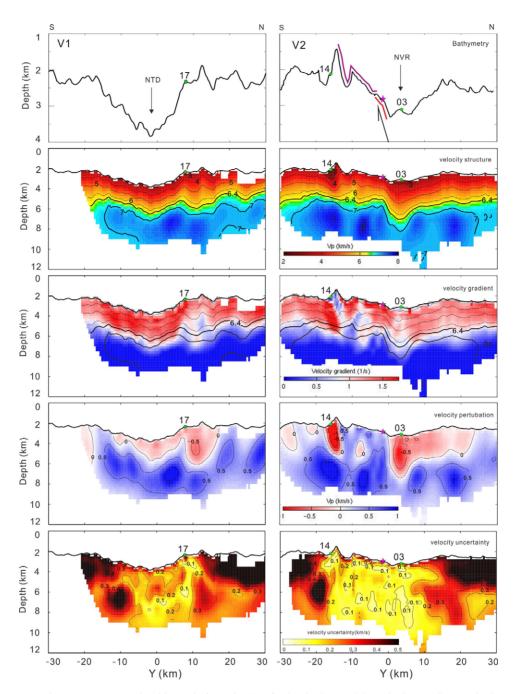
Figure 5. Four sections transverse to the ridge axis from the 3-D final velocity models, velocity gradient, velocity anomaly, and velocity uncertainty model (locations are shown in Figure 2). Masked (white) regions correspond to lack of ray coverage. The pink star in section V2 indicates the location of the active Dragon Flag vent. Green circles are the positions of OBSs. Velocity contours are shown every 1.0 km/s. The 6.4 and 7.0 km/s velocity contours are shown as bold contours. Two bold red lines in V3 velocity section are corresponding to two bold red lines in Figure 8 determined by *PmP*. The three vertical lines in the V5 section represent the locations of three 1-D models in Figure 9b. The velocity contours are plotted over the velocity gradient color maps for comparison. The oceanic detachment faults (ODF) are marked by heavy solid purple lines and termination scarps are marked by heavy red lines on bathymetry profiles.

characterize seismic layers [*Tong et al.*, 2003]. Velocity anomalies are derived by subtracting the average 1-D ensemble (Figure S1 in supporting information) from the final average ensemble for each node of the velocity model. Velocity uncer-

tainties are the statistical standard deviation of the 100 valid solutions. As expected, the edges of the model have large uncertainties (>0.3 km/s) due to a decreased number of crossing rays in these areas. The central part of the preferred 3-D model is well
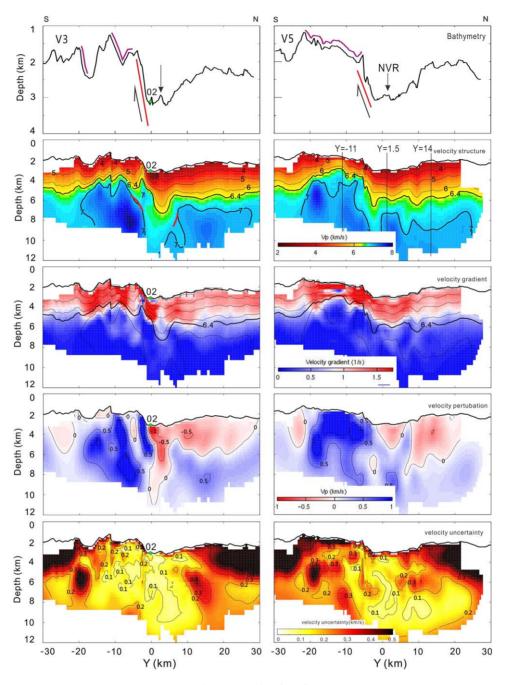
Figure 5. (Continued)

constrained, velocities there have standard deviation <0.2 km/s (Figures 5 and 6), smaller than the variance of the initial models used in the Monte Carlo approach (supporting information Figure S1).

4.3. Crustal Structure Along Line Y3Y4

[19] Profile Y3Y4 is closely perpendicular to the spreading ridge of segment 28. The four OBS spaced every 10 km along this profile all

recorded clearly seismic phases with high quality (Figure 1). Data from OBS2 are taken as an example to constrain the Moho interface (Figure 8). *PmP*, reflected from Moho interface, is recorded clearly at 5–12 km offset at the left half branch and 13–15 km at the right half branch; *Pn*, refracted from the upper mantle, is likewise displayed as far as 35 km offset with an apparent velocity of 8.0 km/s (Figure 8a). We used the ray trace modeling and inversion approach [*Zelt and*
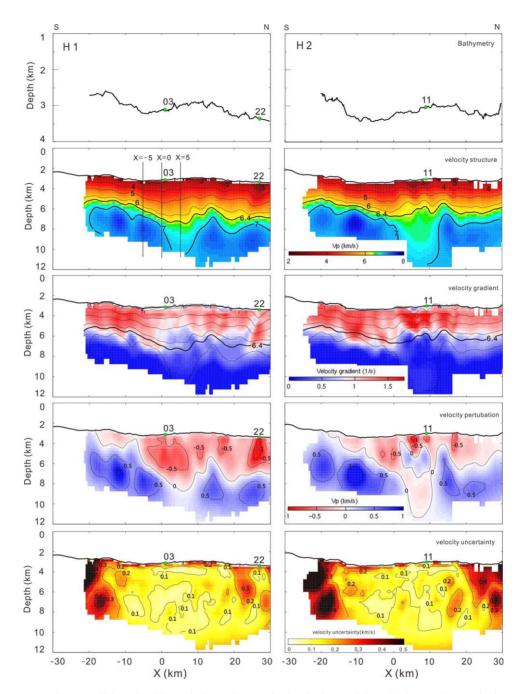
Figure 6. Four sections parallel to the ridge axis from the 3-D final velocity models, velocity gradient, velocity anomaly, and velocity uncertainty model (locations shown in Figure 2). The three vertical lines in the H1 section represent the locations of three 1-D models in Figure 9a. Other symbols are as in Figure 5.

Smith, 1992] to obtain a 2-D model along the Y3Y4 profile. A strong lateral variation in crustal structure is present in the velocity model along the shooting line Y3Y4 (Figure 8d). The upper crust (layer 2) and lower crust (layer 3) are defined based on the significant change in velocity gradient at the boundary between these two seismic layers. We use low velocities ($\sim$2.5–5.5 km/s) and high-velocity gradients ($>$1–2 s^{-1}) to determine Layer

2 [e.g., *Harding et al.*, 1993]; whereas Layer 3 is characterized by higher velocities ($\sim$6.4–7.0 km/s) and lower-velocity gradients ($<$1 s^{-1}).

[20] The 2-D model presents a strong asymmetry across the ridge axis (Figure 8d) as well as illustrated by the V2 section in Figure 5. A similar structure has been observed at other ridge segments. For example, the seismic structure at MAR
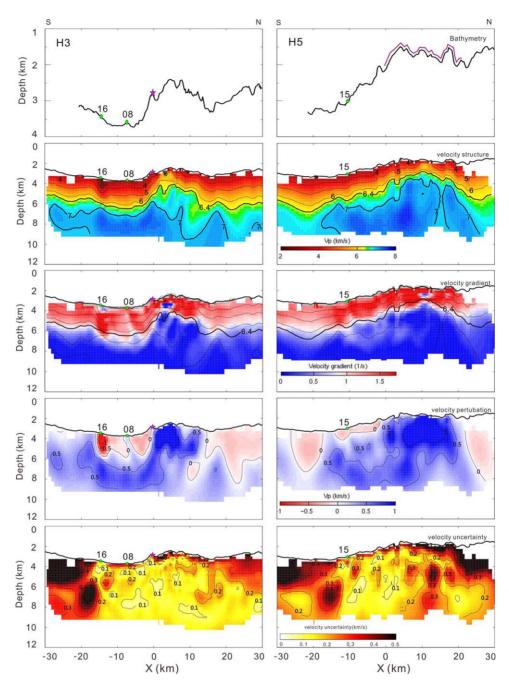
Figure 6.   (Continued).

at 22°19′N yielded a profound difference between conjugated ridge flanks in the presence of a detachment fault [*Dannowski et al.*, 2010]. Both the MAR and SWIR experiments observed *PmP* arrivals, which indicate that an impedence contrast exists at the Moho interface.

4.4.   Tomographic Velocity Model Results

[21] We use the velocity, velocity gradient, and velocity anomaly models to propose a subdivision of the oceanic crust into layers although there is no interface information in our tomography model. The 6.4 km/s velocity contour, corresponding to the sharpest change in velocity gradient, generally coincides with the layer 2–layer 3 boundary [e.g., *Muller et al.*, 1997; *Minshull and White*, 1996]. We tentatively identify the 7.0 km/s velocity contour in our tomography model as the bottom of layer 3 based on of the structure along line Y3Y4 presented in the previous section (Figure 8).

[22] The NTD domain between segments 28 and 29 (Figure 5) shows low-velocity and high-
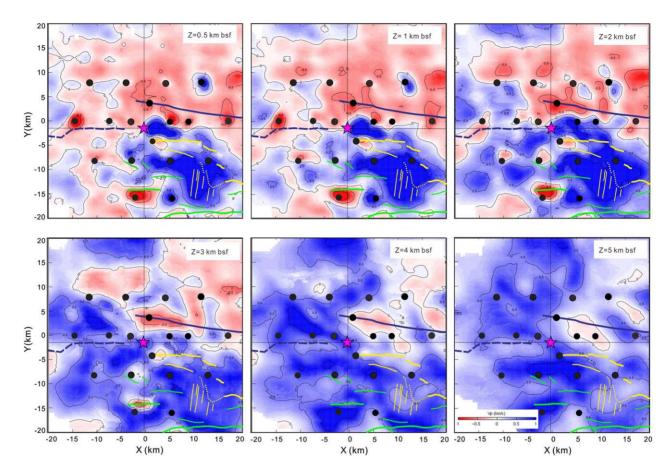
Figure 7. Sections at constant depths below the seafloor from the velocity anomaly models. Other symbols are as in Figure 2.

velocity gradient in the V1 section that crosses the western NTD basin (Figure 5a), where the thicknesses of layer 2 and 3 are <3.0 and <1.0 km, respectively.
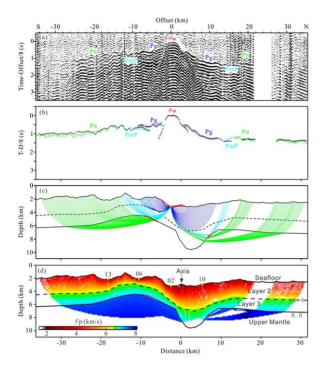
[23] Sections V2 to V6 crosscut the more central part of segment 28. All of these profiles present a pronounced across-axis asymmetry in crustal velocity structure (Figure 5 and Figure S2 in supporting information) with the southern ridge flank characterized by higher seismic velocity (>6.4 km/s) at shallow depths ($Z \leq 2$ km bsf; Figure S4). For section V2 (Figure 5a), the thicknesses of crustal layers 2 and 3 are of 2.2 and 0.8 km, respectively, in the southern ridge flank (at $y = 3$ km); 4.0 and 1.2 km beneath the NVR (at $y = 0$ km); and 2.8 and 0.9 km in the northern ridge flank (at $y = 10$ km). The Dragon Flag vent in Section V2 is located at the boundary between the domains of anomalously low and anomalously high in the velocity perturbation models (Figure 5a). The location of this vent field also coincides with the emergence of the inferred termination fault of this OCC (Figures 2, 5, and 7). The V2

profile also shows anomalously low velocities next to the steep relief interpreted as a breakaway structure (near OBS14; Figure 5a). This low velocity could be due to enhanced fracturing of the uppermost crust and/or to the presence of basalts next to the breakaway.

[24] The OCC domal structure with thinner crust and higher upper crustal velocities is fully developed in sections V4 and V5 that cross over the corrugated central part of the dome (Figures 2 and 5b). Three 1-D velocity models are extracted from section V5 in order to illustrate the along flow line variability (Figure 9b). The core of the OCC (V5 section at $y = -11$ km) is characterized by a seafloor velocity of 4.5 km/s and crustal thickness of 2.6 km. The 1-D velocity profile in the north flank (profile V5, $y = 14$ km; Figure 9b) has the features of normal oceanic crust [*White et al.*, 1992], and is similar to the 1-D profile at the ridge axis (profile V5, $y = 1.5$ km; Figure 9b).

[25] In the along-axis direction, 3-D tomographic slices show significant lateral variations of P wave

Figure 8. (a) OBS02 seismic record section along Y3Y4 line, whose location is shown in Figure 1; (b) observed travel time curves (colored vertical bar with length equal to the assigned travel time uncertainty) and calculated travel time curves (black broken lines) of OBS02, different colors mean the travel times for different kinds of seismic phases; (c) ray tracing and model simulation; the different paths is correspond to different kinds of seismic phases; (d) 2-D velocity model along Y3Y4 shooting line from forward ray tracing.

velocity (Figure 6 and Figure S3 in supporting information). The crustal thickness decreases systematically from the segment center toward the segment ends. This pattern is clearly shown in sections H1 and H2 (Figure 6a) that are located on top (H1) and just to the south (H2) of the NVR. In the H1 section, the thickness of layer 2 along axis based on the 6.4 km/s contour changes from 2.5 km at the western NTD (e.g., at $x = -5$ km; Figure 9a) to 4.2 km at the segment center (e.g., at $x = 5$ km; Figure 9a). The thickness of layer 3 (inferred to be limited by the 7 km/s isovelocity contour) in H1 section also varies from about 0.7 km at the western NTD to about 2.8 km at the segment center (Figure 9a). In section H2, the 7 km/s contour at the segment center is significantly deeper than in other sections (Figure 6), yielding an inferred crustal thickness of 8 km (Figure 10). This tendency is also visible in the plan view depth slices (Figure 7), where a low-velocity zone is parallel to the ridge axis with high-velocity gradient and low-velocity anomaly coinciding with the NVR (e.g., at 3 and 4 km bsf in Figure 7). Sections (from H3 to H6) all cross the OCC domain. Sec-

tion H5 shows the strongest lateral changes, with substantial crustal thinning in a broad domal region centered at $x = 10$ km (Figure 6b), where the model crust is only ~2 km thick with high velocities (>4.5 km/s) at the seafloor.

[26] In plan view, this domain of high seismic velocity perturbation in the shallow crust (Figure 7) coincides with the OCC region determined from the bathymetric data (Figure 2). The highest velocities in the 0.5–2 km bsf slices correspond with the core region of the dome, including the corrugated area, and to the axial valley wall against the inferred termination fault and next to the Dragon Flag vent field (Figure 7).

5. Discussion

5.1. Crustal Thickness Variations

[27] The thickness at the center of segment 28 is greater than at the ends of the segment. Using the 7.0 km/s isovelocity contour as a reference for the base of the crust, the average crustal thickness varies from 3.0 to 4.0 km at the western end of segment 28 to 7.0–8.0 km beneath the NVR at the ridge segment center (sections H1 and H2; Figures 6a, 9a, and 10). The along-axis crustal thickness variation profiles fit well the gravity-derived crustal pattern, showing on average 2–3 km thicker crust at segment center than at the NTDs [*Mendel et al.*, 2003; *Sauter et al.*, 2004]. This range of crustal thickness variations is similar to that documented by *Muller et al.* [1999] and *Minshull et al.* [2006] to the east of the Melville Fracture zone (66°E), where crustal thickness varies from 5 to 6 km at segment midpoints to ~3 km at segment ends [*Minshull et al.*, 2006]. The thick layer 3 (with generally 6.4–7.0 km/s velocities) at the ridge center, is clearly anomalous (Figures 6a) in thickness (2.8–5.0 km). This observed low-velocity zone suggests that magmatic accretion is focused at the segment center forming a thicker crustal root there (Figure 10). We thus disagree with a previous interpretation of the segmentation where segment 28 was fed laterally from segment 27 [*Sauter et al.*, 2001].

[28] The overall crustal thickness beneath the NVR (~5–8.0 km) is greater than that beneath the OCC in the southern ridge flank (~3.0–4.0 km) and greater than or equal to the crust beneath the northern ridge flank (~5.0 km) (V2–V5 sections; Figures 7 and 10). This could indicate that the ridge is currently at a stage of enhanced magmatic

Geochemistry
Geophysics
Geosystems

G^3

ZHAO ET AL.: 3-D SEISMIC STRUCTURE OF DRAGON FLAG OCC
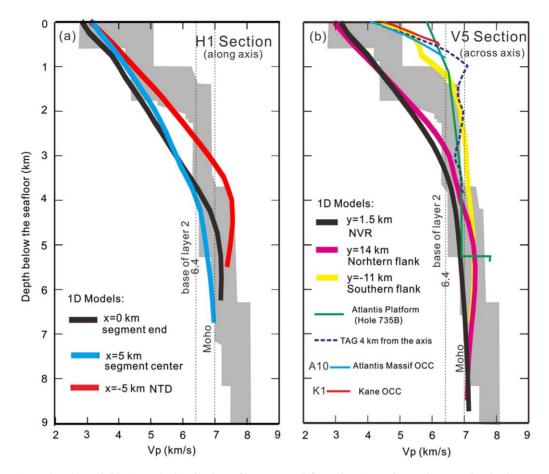
10.1002/ggge.20264

Figure 9. (a) and (b) 1-D velocity-depth profiles extracted from the H1 section and V5 section in the pre-ferred model for parallel and perpendicular to axis, respectively. For comparison, 1-D velocity profiles from other locations within several OCCs are shown: Atlantis Platform profile from *Muller et al.* [1997] at location of ODP Hole 735B; TAG 1D model extracted at 4 km east from the axis along Profile 2 of *Canales et al.* [2007]; Atlantis Massif OCCs and Kane OCCs from *Canales et al.* [2008], whose solid lines are extracted from a high shallow velocity portion and appearing "normal" velocity of the same model, respectively. Shaded backgrounds show, for reference purposes, the compilation of profiles in 1–7 Ma Atlantic crust of *White et al.* [1992].

activity, possibly with focused partial melting in the lower crust [*Sauter et al.*, 2009]. The seismic crustal thickness in our tomography model is com-parable to the crustal thickness modeled from the gravity data [*Mendel et al.*, 2003]. The maximum thickness in the gravity-derived model [*Mendel et al.*, 2003] is located a few km to the north of the NVR, while it is just south of the NVR in our seis-mic model (Figure 10). This discrepancy is most probably an artifact of the gravity inversion and therefore not geologically significant.
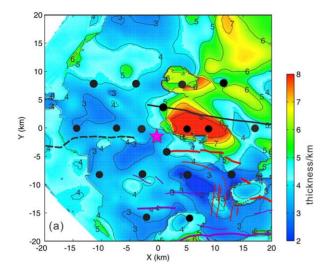
5.2. The Dragon Flag OCC Structure and Nature

[29] Our seismic images in the across-axis sections present a strong asymmetry associated with an

OCC in the southern ridge flank (Figure 5). We combined the multibeam bathymetry data with our images at depth together to analyze the Dragon Flag OCC structure. Our results show striking con-sistency between surface topography features of the OCC and Vp patterns. The OCC structure is characterized by a crustal thickness of ∼2.0–3.0 km and velocities with ∼0.5–2.0 km/s higher than that of average oceanic crust in the shallow crust (Figures 5b, 7, and 9b). The corrugated portions of the OCC (Figures 2 and 5–7) coincide with the thinnest crust and highest upper crustal velocities. This recalls the seismic velocity structure of other OCCs: Atlantis Massif [*Canales et al.*, 2008] where gabbros have been recovered in Integrated Ocean Drilling Program (IODP) cores [*Blackman et al.*, 2006], and TAG [*Canales et al.*, 2007; *Zhao*

Figure 10. Crustal thickness map calculated as depth to the 7.0 km/s isovelocity contour minus the depth at seafloor in 3-D model. Other symbols are as in Figure 2.

et al., 2012] where gabbros have been recovered in dredge hauls [Zonenshain et al., 1989]. Comparison of the extracted 1-D models in Figure 9b shows that the shallow high-velocity body is similar in structure to the Kane OCC [Canales et al., 2008] and the one at Atlantis Massif [Henig et al., 2012]. Gabbros have been sampled at the OCCs, at least in its corrugated core region, at Atlantis

Bank (ODP Hole 735B), close to the Kane TF (remotely operated vehicle (ROV) observations and sampling) and at Atlantis Massif (IODP Hole U1309D) suggesting gabbroic cores for these massifs [Dick et al., 2000; Blackman et al., 2006]. Based on these comparisons, we might conclude that the OCC in segment 28 is dominated by gabbro, and perhaps diabase (since gabbros and diabase have similar seismic velocity ranges [Miller and Christensen, 1997]). Actually two dredge hauls in the termination area (dredges 74 and 76 in Figure 2) among five dredges of the Edul cruise [Mével et al., 1997] recovered only basalts. However this do not contradict with our reasoning because dredges on corrugated surfaces commonly recover basalt rubbles left from hanging wall blocks [Searle et al., 2003]. The variations of OCC images along flow line (Figure 5) fit very well with the conceptual model proposed by Cannat et al. [2009] for the switch from dome to termination in the east of Melville area, which presents the velocities of the upper footwall (the rigidity of the axial plate) varying more or less during the different phases of OCC formation.

[30] Combined with the interpretation of the bathymetric data (Figure 2), our seismic results allow to image both the corrugated portions of the
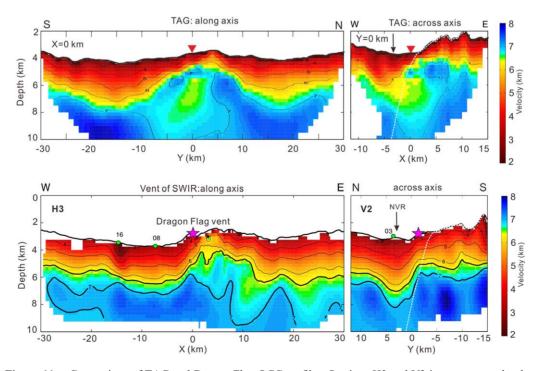

Figure 11. Comparison of TAG and Dragon Flag OCC profiles. Sections H3 and V2 intersect at each other at the location of the active Dragon Flag hydrothermal vent (purple star). TAG sections $X = 0$, $Y = 0$ are from Zhao et al. [2012]. The white dash lines show the detachment faults.
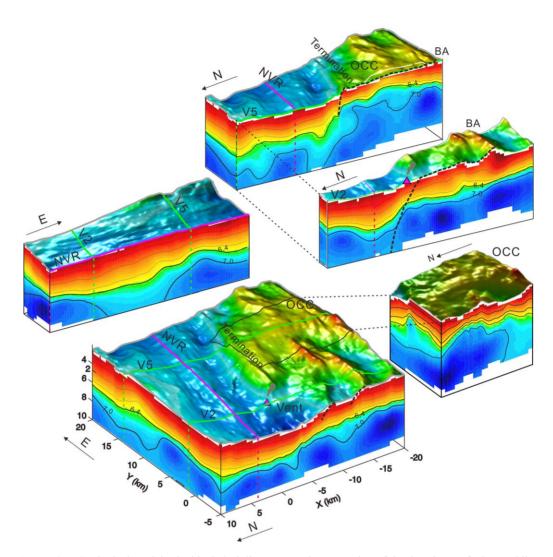
Figure 12. Geological model. The black dash lines are our interpretation of the detachment faults. Red lines indicate NVR and corresponds to the H1 section in Figure 6. The red triangle indicates the location of the Dragon Flag vent. The V2 and V5 green lines show the location of the V2 and V5 sections in Figure 5, respectively.

detachment fault surface exhumed at the seafloor and the remaining hidden parts which cannot be mapped solely with the bathymetric data. We propose that the oceanic detachment faults (ODFs) of segment 28, includes the corrugated top surface of the OCC, and extents from the breakaway at the south (bold purple lines in Figure 2) to the high-angle termination fault to the north (bold red lines in Figure 2). It is cut by many short-lived faults. The ODF extend ~25 km long along axis and ~20 km wide along flow line between the breakaway and termination faults (e.g., $Z = 2$ km bsf in Figure 7). This larger extent of the ODF relative to the small size of the corrugated area (6 km by 5 km) observed in the bathymetry is consistent with the idea that ODF distribution is larger than estimation on the basis of the distribution of corru-

gated domes. The high-velocity body at the center of the H3 section (Figures 6 and 11) may be interpreted as the core of the OCC which may be of primarily gabbroic composition. The exhumed detachment fault in the southern flank of segment 28 has therefore a complex 3-D structure (Figure 12) with variable dips both along flow line, indicating temporal variations of the ODF dip as it emerged from the seafloor, and perpendicular to flow lines indicating along-axis variations of the ODF geometry. Our results also support an idea that detachment faulting plays a major role in oceanic crust accretion, not only in a moderate to reduced magma supply context, which was already deduced from studies at the MAR [*Tucholke et al.*, 2008; *Escartín et al.*, 2008], but also in relatively robust magmatic ridge sections.

5.3. The Dragon Flag Hydrothermal Vent Field

[31] The active Dragon Flag vent field is located in the western part of ridge segment 28, at the boundary between the lower and higher velocity bodies imaged near the OCC termination fault (Figures 5–7). A large positive velocity perturbation is well marked in the shallow crust near the hydrothermal vent field (at $Z = 0.5, 1, 2$ km bsf in Figure 7, sections V2 and V3 in Figure 5), yet this field is located on a basaltic basement. The across-axis bathymetric, gravimetric [*Mendel et al.*, 2003] and seismic velocity asymmetry in the V2 section (Figures 5 and 10) extends off axis at least 16 km to the south, indicating that detachment faulting and uplifting of deep lithologies have been occurring here for at least the last ~2.0 Myr (assuming a total spreading rate of 14 mm/yr). This is similar to the time range of formation for other OCCs [*Tucholke et al.*, 1998]. These long-lived ODFs are thought to provide pathways for hydrothermal circulation [*Zhang et al.*, 2013], a model that has been proposed for hydrothermal circulation at TAG (Figure 11). The geometry of the domed detachment fault of TAG inferred from microseismicity and seismic models [*deMartin et al.*, 2007; *Canales et al.*, 2007; *Zhao et al.*, 2012] roots at a steep angle ~60° [*deMartin et al.*, 2007] and rotates to smaller angles in the upper crust. Future work on the distribution of micro-earthquakes will provide further constrains on the detachment fault geometry in the area of the Dragon Flag vent field.

[32] The dip of the ODF in the subsurface and the distance from the vent are similar both at the TAG and at the Dragon Flag vent fields. However, the heat sources driving hydrothermal circulation may be different. There is a relatively low-velocity domain in the footwall beneath the TAG vent field (Figure 11) that may represent a domain with melt present and therefore act as a heat source within the ODF footwall [*Zhao et al.*, 2012]. There is no such low-velocity zone beneath the Dragon Flag vent field (Figure 11), whose heat source may thus come from deeper, or lateraly from the more magmatically robust NVR region to the east (Figure 10) which could drive hydrothermal circulation there.

6. Conclusions

[33] 3-D tomographic inversion for the first arrivals yielded lateral variation of P wave velocity along the axis. The crustal thickness, constrained by the 7 km/s isocontour line, decreases systematically from the center of ridge segment 28 (~7.0–8.0 km) toward the segment ends (~3.0–4.0 km). Layer 2 with a strong velocity gradient remains relatively constant in thickness, and Layer 3 corresponding to a low-velocity gradient, changes greatly from the segment ends to the segment center. The crustal thickness is comparable to that of the gravity-derived model. These along-axis variations of P wave velocity and thickness lead to the conclusion that the magmatic activity is focusing at the segment center.

[34] Our 3-D P wave velocity model also shows that structural asymmetrical accretion involving an ODF. On the basis of multibeam bathymetry data, the Dragon Flag OCC (6 km by 5 km) discovered with a corrugated central domain in the southern flank of the ridge, is consistent with a domain of thin crust and high shallow crustal velocities. Similarities with domains of gabbro exhumation at the MAR (close to Kane TF and at the Atlantis Massif) suggest that these high shallow crustal velocities and thin crust domains correspond to plutonic rocks. The ODFs with larger extent (25 km by 20 km) than the size of OCC suggests that the distribution of ODFs is wider than though before. These results lead to the conclusion that the ODFs play a major role in oceanic crustal accretion in relatively robust magmatic segment, which were once testified to be critical in moderate to reduced magma supplied segment at the MAR [*Tucholke et al.*, 2008; *Escartín et al.*, 2008].

[35] Associated closely with the ODF, hydrothermal activities were identified in the study region. We propose that this long-lived detachment fault provides the pathway for the Dragon Flag hydrothermal circulation. Based on the 3-D model and crustal thickness anomaly, the heat source of this vent that drives hydrothermal convection may be the magmatically robust axial region beneath the center of the ridge segment, to the northeast of the Dragon Flag vent field.

Acknowledgments

References

Ao, W., M. H. Zhao, X. L. Qiu, J. B. Li, A. G. Ruan, and J. Z. Zhang (2010), The correction of shot and OBS position in the 3D seismic experiment of the SW Indian Ocean Ridge, *Chin. J. Geophys.*, 53, 1072–1081.

Baker, E. T., and C. R. German (2004), On the global distribution of hydrothermal vent fields, in Mid-Ocean Ridges: Hydrothermal Interactions Between the Lithosphere and Oceans, edited by C. R. German, J. Lin, and L. M. Parson, p. 245–266, AGU, Washington, D. C.

Blackman, D. K., B. Ildefonse, B. E. John, Y. Ohara, D. J. Miller, C. J. MacLeod, and Expedition 304/305 Scientists (2006), *Oceanic core complex formation*, Atlantis massif, Proc. Integrated Ocean Drill. Program, 304/305, doi:10.2204/iodp.proc.304305. 2006. College Station, Tex.

Canales, J. P., R. A. Sohn, and B. deMartin (2007), Crustal structure of the Trans-Atlantic Geotraverse (TAG) segment (Mid-Atlantic Ridge, 26°10′N): Implications for the nature of hydrothermal circulation and detachment faulting at slow spreading ridges, *Geochem. Geophys. Geosyst.*, 8, Q08004, doi:10.1029/2007GC001629.

Canales, J. P., B. E. Tucholke, M. Xu, J. A. Collins, and D. L. Dubois (2008), Seismic evidence for large-scale compositional heterogeneity of oceanic core complexes, *Geochem. Geophys. Geosyst.*, 9, Q08002, doi:10.1029/2008GC002009.

Cann, J. R., D. K. Blackman, D. K. Smith, E. McAllister, B. Janssen, S. Melle, E. Avgerinos, A. R. Pascoe, and J. Escartin (1997), Corrugatedslip surface formed at ridge-transform intersections on the Mid-Atlantic Ridge, *Nature*, 385, 329–332.

Cannat, M. (1993), Emplacement of mantle rocks in the seafloor at mid-ocean ridges, *J. Geophys. Res.*, 98, 4163–4172.

Cannat, M., C. Rommevaux-Jestin, D. Sauter, C. Deplus and V. Mendel (1999), Formation of the axial relief at the very slow spreading Southwest Indian Ridge(49° to 69°E), *J. Geophys. Res.*, 104, 22,825–22,843.

Cannat, M., D. Sauter, V. Mendel, E. Ruellan, K. Okina, J. Escartin, V. Combier, and M. Baala (2006), Mode of seafloor generation at a melt-poor ultraslow-spreading ridge, *Geology*, 34, 605–608.

Cannat, M., D. Sauter, A. Bezos, C. Meyzen, E. Humler and M. Le Rigoleur (2008), Spreading rate, spreading obliquity, and melt supply at the ultraslow spreading Southwest Indian Ridge, *Geochem. Geophys. Geosyst.*, 9, Q04002, doi:10.1029/2007GC001676.

Cannat, M., D. Sauter, J. Escartin, L. Lavier and S. Picazo (2009), Oceanic corrugated surfaces and the strength of the axial lithosphere at slow spreading ridges, *Earth Planet. Sci. Lett.*, 288, 174–183.

Chu, D., and R. G. Gordon (1999), Evidence for motion between Nubia and Somalia along the Southwest Indian Ridge, *Nature*, 398, 64–67.

Dannowski, A., I. Grevemeyer, C. R. Ranero, G. Ceuleneer, M. Maia, J. P. Morgan, and P. Gente (2010), Seismic structure of an oceanic core complex at the Mid-Atlantic Ridge, 22°19′N, *J. Geophys. Res.*, 115, B07106, doi:10.1029/2009JB006943.

Debayle, E., B. Kennett, and K. Priestley (2005), Global azimuthal seismic anisotropy and the unique plate-motion deformation of Australia, *Nature*, 433(7025), 509–512, doi:10.1038/nature03247.

deMartin, B. J., R. Reves-Sohn, J. P. Canales, and S. E. Humphris (2007), Kinematics and geometry of active detachment faulting beneath the Trans-Atlantic Geotraverse (TAG) hydrothermal field on the Mid-Atlantic Ridge, *Geology*, 35(8), 711–714.

Dick, H. J. B., et al. (2000), A long in situ section of the lower ocean crust: Results of ODP Leg 176 drilling at the Southwest Indian ridge, *Earth Planet. Sci. Lett.*, 179, 31–51, doi:10.1016/S0012-821X(00)00102-3.

Dick, H. J. B., J. Lin, and H. Schouten (2003), An ultraslow-spreading class of ocean ridge, *Nature*, 426, 405–412.

Escartín, J., and J. P. Canales (2011), Detachments in oceanic lithosphere: Deformation, magmatism, fluid flow and ecosystems, *Eos Trans. AGU*, 92(4), 31.

Escartín, J., D. K. Smith, J. Cann, H. Schouten, C. H. Langmuir, and S. Escrig (2008), Central role of detachment faults in accretion of slow-spreading oceanic lithosphere, *Nature*, 455, 790–794.

Georgen, J. E., J. Lin, and H. J. B. Dick (2001), Evidence from gravity anomalies for interactions of the Marion and Bouvet hotspots with the Southwest Indian Ridge: Effects of transform offsets, *Earth Planet. Sci. Lett.*, 187, 283–300.

German, C. R., E. T. Baker, C. A. Mevel, K. Tamaki, and the FUJI Scientific Team (1998), Hydrothermal activity along the South West Indian Ridge, *Nature*, 395, 490–493, doi:10.1038/26730.

Harding, A. J., G. M. Kent, and J. A. Orcutt (1993), A multichannel seismic investigation of the upper crustal structure at 98N on the East Pacific Rise: Implications for crustal accretion, *J. Geophys. Res.*, 98, 13,925–13,944.

Henig, A. S., D. K. Blackman, A. J. Harding, J. P. Canales, and G. M. Kent (2012), Downward continued multichannel seismic refraction analysis of Atlantis Massif oceanic core complex, 30°N, Mid-Atlantic Ridge, *Geochem. Geophys. Geosyst.*, 13, Q0AG07, doi:10.1029/2012GC004059.

Humphris, S. E., and M. C. Kleinrock (1996), Detailed morphology of the TAG active hydrothermal mound: Insights into its formation and growth, *Geophys. Res. Lett.*, 23, 3443–3446.

Karson, J. A., and R. M. Lawrence (1997), Tectonic setting of serpentinite exposures on the western median valley wall of the MARK area in the vicinity of site 920, in *Proceedings of the Ocean Drilling Program Scientific Results*, vol. 153, edited by J. A. Karson et al., pp. 5–21, Ocean Drill. Program, College Station, Tex.

Karson, J. A., et al. (1987), Along-axis variations in seafloor spreading in the MARK area, *Nature*, 328, 681–685.

Korenaga, J., W. S. Holbrook, G. M. Kent, P. B. Kelemen, R. S. Detrick, H.-C. Larsen, J. R. Hopper, and T. Dahl-Jensen (2000), Crustal structure of the southeast Greenland margin from joint refraction and reflection seismic tomography, *J. Geophys. Res.*, 105, 21,591–21,614.

Mendel, V., D. Sauter, C. Rommevaux-Jestin, P. Patriat, and F. Lefebvre (2003), Magmato-tectonic cyclicity at the ultraslow spreading Southwest Indian Ridge: Evidence from variations of axial volcanic ridge morphology and abyssal hills pattern, *Geochem. Geophys. Geosyst.*, 4(5), 9102, doi:10.1029/2002GC000417.

Mével, C., et al. (1997), Sampling the Southwest Indian Ridge: First results of the EDUL cruise (R/V Marion Dufresne II, August 1997), *InterRidge News*, 6, 25–26.

Miller, D., and N. Christensen (1997), Seismic velocities of lower crustal and upper mantle rocks from the slow-spreading Mid-Atlantic Ridge, south of the Kane transform zone (MARK), in *Proceedings of the Ocean Drilling Program Scientific Results*, vol. 153, edited by J. A. Karson et al., pp. 437–454, Ocean Drill. Program, College Station, Tex.

Minshull, T. A., and R. S. White (1996), Thin crust on the flanks of the slow-spreading Southwest Indian Ridge, *Geophys. J. Int.*, 125(1), 139–148.

Minshull, T. A., M. R. Muller, and R. S. White (2006), Crustal structure of the Southwest Indian Ridge at 66°E: Seismic constraints, *Geophys. J. Int.*, *166*, 135–147.

Muller, M. R., C. J. Robinson, T. A. Minshull, R. S. White, and M. J. Bickle (1997), Thin crust beneath ocean drilling program borehole 735B at the Southwest Indian Ridge?, *Earth Planet. Sci. Lett.*, *148*, 93–107.

Muller, M. R., T. A. Minshull, and R. S. White (1999), Segmentation and melt supply at the Southwest Indian Ridge, *Geology*, *27*(10), 867–870.

Muller, M. R., T. A. Minshull, and R. S. White (2000), Crustal structure of the Southwest Indian Ridge at the Atlantis II Fracture Zone, *J. Geophys. Res.*, *105*, 25,809–25,828.

Olive, J. A., M. D. Behn, and B. E. Tucholke (2010), The structure of oceanic core complexes controlled by the depth distribution of magma emplacement, *Nat. Geosci.*, *3*, 491–495.

Patriat, P., et al. (1996), The GALLIENI cruise: A geophysical survey of the Southwest Indian Ridge near the Gallieni FZ (37°S, 52°E), *InterRidge News*, *5*, 19–22.

Patriat, P., D. Sauter, M. Munschy, and L. M. Parson (1997), A survey of the Southwest Indian Ridge axis between Atlantis II Fracture Zone and the Indian Triple Junction: Regional setting and large scale segmentation, *Mar. Geophys. Res.*, *19*, 457–480.

Rommevaux-Jestin, C., C. Deplus, and P. Patriat (1997), Mantle Bouguer anomaly along an ultra slow-spreading ridge: Implications for accretionary processes and comparison with results from central Mid-Atlantic Ridge, *Mar. Geophys. Res.*, *19*, 481–503.

Rona, P. A., G. Klinkhammer, T. A. Nelsen, J. H. Trefry, and H. Elderfield (1986), Black smokers, massive sulfides and vent biota at the mid-Atlantic Ridge, *Nature*, *321*, 33–37.

Sauter, D., P. Patriat, C. Rommevaux-Jestin, M. Cannat, A. Briais, and Gallieni Shipboard Scientific Party (2001), The Southwest Indian Ridge between 49°15′E and 57°E: Focused accretion and magma redistribution, *Earth Planet. Sci. Lett.*, *192*, 303–317.

Sauter, D., H. Carton, V. Mendel, M. Munschy, C. Rommevaux-Jestin, J. Schott, and H. Whitechurch (2004), Ridge segmentation and the magnetic structure of the ultraslow Southwest Indian Ridge (at 50°30′E, and 50°30′E and 66°20′E): Implications for magnetic processes at ultraslow-spreading centers, *Geochem. Geophys. Geosyst.*, *5*, Q05K08, doi:10.1029/2003GC000581.

Sauter, D., M. Cannat, C. Meyzen, A. Bezos, P. Patriat, E. Humler, and E. Debayle (2009), Propagation of a melting anomaly along the ultraslow Southwest Indian Ridge between 46°E and 52°20′E: Interaction with the Crozet hotspot?, *Geophys. J. Int.*, *179*, 687–699.

Searle, R. C., M. Cannat, K. Fujioka, C. Mével, H. Fujimoto, A. Bralee, and L. Parson (2003), FUJI Dome: A large detachment fault near 64°E on the very slow-spreading southwest Indian Ridge, *Geochem. Geophys. Geosyst.*, *4*(8), 9105, doi:10.1029/2003GC000519.

Seyler, M., M. Cannat, and C. Mével (2003), Evidence for major-element heterogeneity in the mantle source of abyssal peridotites from the Southwest Indian Ridge (52° to 69°E), *Geochem. Geophys. Geosyst.*, *4*(2), 9101, doi:1029/2002GC000305.

Smith, D. K., J. R. Cann, and J. Escartín (2006), Widespread active detachment faulting and core complex formation near 13°N on the Mid-Atlantic Ridge, *Nature*, *442*, 440–443.

Smith, D. K., J. Escartín, H. Schouten, and J. R. Cann (2008), Fault rotation and core complex formation: Significant processes in seafloor formation at slow-spreading mid-ocean ridges (Mid-Atlantic Ridge, 13°-15°N), *Geochem. Geophys. Geosyst.*, *9*, Q03003, doi:10.1029/2007GC001699.

Tao, C. H., et al. (2012), First active hydrothermal vents on an ultraslow-spreading center: Southwest Indian Ridge, *Geology*, *40*, 47–50, doi:10.1130/G32389.1.

Tong, C. H., et al. (2003), Influence of enhanced melt supply on upper crustal structure at a mid-ocean ridge discontinuity: A three dimensional seismic tomographic study of 9°N East Pacific Rise, *J. Geophys. Res.*, *108*(B10), 2464, doi:10.1029/2002JB002163.

Tucholke, B. E., and J. Lin (1994), A geological model for the structure of ridge segments in slow spreading ocean crust, *J. Geophys. Res.*, *99*, 11,937–11,958.

Tucholke, B. E., J. Lin, and M. C. Kleinrock (1998), Megamullions and mullion structure defining oceanic metamorphic core complexes on the Mid-Atlantic Ridge, *J. Geophys. Res.*, *103*, 9857–9866.

Tucholke, B. E., M. D. Behn, R. Buck, and J. Lin (2008), The role of melt supply in oceanic detachment faulting and formation of megamullions, *Geology*, *36*(6), 455–458.

White, R. S., D. McKenzie, and R. K. O'Nions (1992), Oceanic crustal thickness from seismic measurements and rare earth element inversions, *J. Geophys. Res.*, *97*, 19,683–19,715.

Zelt, C. A., and P. J. Barton (1998), Three-dimensional seismic refraction tomography: A comparison of two methods applied to data from the Faeroe Basin, *J. Geophys. Res.*, *103*, 7187–7210.

Zelt, C. A., and D. A. Forsyth (1994), Modeling wide-angle seismic data for crustal structure: Southeastern Grenville Province, *J. Geophys. Res.*, *99*, 11,687–11,704.

Zelt, C. A., and R. B. Smith (1992), Seismic travel time inversion for 2-D crustal velocity structure, *Geophys. J. Int.*, *108*, 16–34.

Zhang, J., U. S. ten Brink, and M. N. Toksöz (1998), Nonlinear refraction and reflection travel time tomography, *J. Geophys. Res.*, *103*, 29,743–29,757.

Zhang, J. Z., M. H. Zhao, X. L. Qiu, A. G. Ruan, J. B. Li, Y. J. Chen, W. Ao, and X. D. Wei (2012), OBS seismic data processing and its preliminary results in the hydrothermal field of the Southwest Indian Ridge, *J. Trop. Oceanogr.*, *31*(3), 79–89.

Zhang, T., J. Lin, and J. Y. Gao (2013), Magmatism and tectonic processes in the area of hydrothermal vent on Southwest Indian Ridge, *Sci. China Earth Sci.*, doi:10.1007/s11430-013-4630-5.

Zhao, M. H., J. P. Canales, and R. A. Sohn (2012), Three-dimensional seismic structure of a Mid-Atlantic Ridge segment characterized by active detachment faulting (TAG, 25°55′N–26°20′N), *Geochem. Geophys. Geosyst.*, *13*, Q0AG13, doi:10.1029/2012GC004454.

Zhu, J., J. Lin, Y. J. Chen, C. Tao, C. R. German, D. R. Yoerger, and M. A. Tivey (2010), A reduced crustal magnetization zone near the first observed active hydrothermal vent field on the Southwest Indian Ridge, *Geophys. Res. Lett.*, *37*, L18303, doi:10.1029/2010GL043542.

Zonenshain, L. P., M. I. Kuzmin, A. P. Lisitsin, Y. A. Bogdanov, and B. V. Baranov (1989), Tectonics of the Mid-Atlantic rift valley between the TAG and MARK areas (26°–24°N): Evidence for vertical tectonism, *Tectonophysics*, *159*, 1–23.